

The [CII]–SFR correlation in dwarf galaxies across cosmic time

Alessandro Lupi¹[★] and Stefano Bovino²

¹*Scuola Normale Superiore, Piazza dei Cavalieri 7, Pisa, IT-56126 Italy*

²*Departamento de Astronomía, Universidad de Concepción, Barrio Universitario, Concepción, Chile*

Accepted XXX. Received YYY; in original form ZZZ

ABSTRACT

Current galaxy observations suggest that a roughly linear correlation exists between the [CII] emission and the star formation rate, either as spatially-resolved or integrated quantities. Observationally, this correlation seems to be independent of metallicity, but the very large scatter does not allow to properly assess whether this is true. On the other hand, theoretical models tend to suggest a metallicity dependence of the correlation. In this study, we investigate the metallicity evolution of the correlation via a high-resolution zoom-in cosmological simulation of a dwarf galaxy employing state-of-the-art sub-grid modelling for gas cooling, star formation, and stellar feedback, and that self-consistently evolves the abundances of metal elements out of equilibrium. Our results suggest that the correlation should evolve with metallicity, in agreement with theoretical predictions, but also that this evolution can be hardly detected in observations, because of the large scatter. We also find that most of the [CII] emission is associated with neutral gas at low-intermediate densities, whereas the highest emissivity is produced by the densest regions around star-forming regions.

Key words: galaxies:formation - galaxies:evolution - galaxies: ISM - ISM:molecules

1 INTRODUCTION

Within hierarchical models of cosmological structure formation, dwarf galaxies are considered to be the building blocks of larger galaxies. Compared to normal spiral galaxies, dwarfs contain less metals (Tremonti et al. 2004; Hunter et al. 2012) and have been often employed as laboratories to explore high-redshift conditions. Whether or not this can help disentangling how stars form under early Universe conditions is, however, far to be understood (see Cowie et al. 1996, for a different paradigm).

High redshift objects are mainly traced via the far-infrared (FIR) emission, which represent the best tool to measure star-formation rates (SFRs) in metal-poor environments. Detecting molecular gas in these objects is, in fact, challenging (Leroy et al. 2011). Low metallicities imply a low dust-to-gas ratio, favouring the penetration of photodissociating photons. The main molecular tracer, CO, is then confined in smaller regions, and surrounded by larger photodissociation regions (PDRs), where the emission of strong metal lines (e.g. [CII] and [OI]) is strong, as also proved by observations of [CII] to CO ratios (e.g. Israel et al. 1996; Madden et al. 1997).

In particular, the 158 μm [CII] transition is the brightest line originating from star-forming galaxies (e.g. Stacey et al. 1991; Brauher et al. 2008), and the dominant coolant for neutral atomic gas (Wolfire et al. 1995, 2003). It has been observed in different types of galaxies, and can also be detected by ALMA in galaxies beyond redshift $z = 6 - 7$ (see e.g. Capak et al. 2015; Maiolino et al. 2015).

Due to its low ionisation potential (11.26 eV), [CII] traces also other regions of the interstellar medium (ISM), as for instance ionised gas components (see e.g. Goldsmith et al. 2012), it is spatially associated with PDR envelopes surrounding CO, and it correlates with the FIR emission, thus tracing the ultraviolet (UV) field strength.

The role of [CII] as star-formation (SF) tracer, has been widely discussed in the literature (De Looze et al. 2014; Herrera-Camus et al. 2015). De Looze et al. (2011) reported a nearly linear correlation between SFR and [CII] luminosity with a dispersion of ~ 0.3 dex for a sample of 24 local, star-forming galaxies, while in a second work (De Looze et al. 2014) based on the Dwarf Galaxy Survey (DGS hereafter) by Madden et al. (2013), they concluded that [OI] 63 μm is a better SF tracer in low-metallicity galaxies. In addition, [CII], normally excited by collision with electrons, atomic, and molecular hydrogen, possesses a lower critical density

[★] E-mail: alessandro.lupi@sns.it

for collisional excitation ($n_{\text{crit}} \sim 10^3 \text{ cm}^{-3}$ ¹), compared to [OI], which then becomes the dominant coolant above those densities (Kaufman et al. 1999).

To understand if [CII] can be used as a universal tracer of the star-forming galaxies across time, we should investigate how its emission and chemistry are connected to the metallicity, the far ultra-violet (FUV) background, and its interaction with dust particles. The metallicity, in particular, is a fundamental parameter as it constrains the amount of dust grains, which have a crucial role for the formation of molecules and in shielding the FUV radiation.

Observational works have also reported the so-called [CII] *line-cooling deficit*, in which the [CII] over the total infrared (TIR) luminosity ratio exhibits large variations. In a recent large survey by Smith et al. (2017) this deficit has been shown within galaxies down to scales of 200 pc. Yet the underlying process (likely local) driving the deficit has not been identified. The impact of harsh radiation in ultra-luminous infrared galaxies (ULIRGs), for instance, might reduce the abundance of small grains and decrease the photoelectric effect (the main heating source), lowering the [CII]/TIR ratio (Luhman et al. 2003). On the other hand, observations of low-metallicity dwarf galaxies (Cormier et al. 2015), have shown opposite behaviour. The lower dust content increases the mean free path of UV photons, causing a UV field dilution over larger spatial scales, which may result in less grain charging, then favouring the photoelectric process.

Together with the [CII] deficit problem, other relevant questions on low-metallicity environments remain open. Determining the role of the different ISM phases on the star formation process, and how these phases are structured are some of those.

[CII] emission can originate from different regions with contributions from molecular, ionised, and atomic phases of the ISM. For these reasons it might also be employed to study the evolution of the ISM from the warm neutral medium to the cold phase, and could help determining the physical conditions of the emitting gas. By studying from where [CII] emission originates and comparing it with typical tracers of other ISM phases, we can help finding an answer to the above questions.

Pineda et al. (2013), via *Herschel* observations of the Galactic plane, have found that dense PDRs are the main sources of the total [CII] emission (~47 per cent), while only ~28 per cent traces CO-dark gas, with most of the emission localised in the spiral arms. Fahrion et al. (2017), via SOFIA observations of the dwarf galaxy NGC 4214, reported that roughly 46 per cent of [CII] emission comes from the HI-dominated medium, while only about 9 per cent of the total [CII] emission can be attributed to the cold neutral medium (CNM). In addition, only 25 per cent of the molecular content can be traced by the [CII].

The observations of FIR lines in high-redshift galaxies by ALMA have also been the motivation for the theoretical/numerical community to start mapping the emission lines in galaxies. However, because of the additional complexity of a proper modelling of non-equilibrium metal chemistry in numerical simulations and the need of very

high resolution, most of the studies to date have relied on post-processing techniques, typically based on photoionisation equilibrium models like Cloudy (Ferland et al. 2013), as in, e.g., Pallottini et al. (2017) and Katz et al. (2019). Unfortunately, this approach cannot properly describe the dynamical evolution of the species, hence the interplay between chemistry and the other physical processes occurring in the galaxy.

The only cases of a proper investigation of the non-equilibrium state of metal species in simulations to date are the studies by Hu et al. (2016, 2017), Hu (2019) and Richings & Schaye (2016). In Hu et al. 2016 papers, they evolved a dwarf galaxy in isolation with an extremely high resolution ($4 M_{\odot}$ per gas particle), employing a simplified network that tracks the primordial species (with only a subset of all the possible ionisation states included) plus only C and O, under the assumption that these metal species can only exist in the molecular form as CO, or separately as C^+ and neutral O. On the other hand, Richings & Schaye (2016) evolved a sub- L^* galaxy in isolation employing a very detailed CO network, with 157 species, but assume a constant metallicity across the entire evolution of the gas. Moreover, isolated galaxy simulations lack the ability to self-consistently track the cosmological evolution of the Universe and the role of environment in shaping to the system under scrutiny, like large-scale inflows and mergers, possibly missing important effects. Here, instead, we build upon our previous study Capelo et al. (2018) and evolve a dwarf galaxy self-consistently in a cosmological context, with the aim to answer a couple of important questions related to [CII] in galaxies: i) is the $158 \mu\text{m}$ [CII] line a valid star formation rate tracer in local galaxies and across time? ii) To which extent [CII] traces different components of the ISM?

2 NUMERICAL SETUP

In this study, we consider the evolution of a dwarf galaxy with a halo mass of $\sim 4 \times 10^{10} M_{\odot}$ at $z = 0$ by means of a zoom-in cosmological simulation performed with the hydrodynamic code GIZMO (Hopkins 2015), descendant from GADGET3 and GADGET2 (Springel 2005). For hydrodynamics, we employ the fully-Lagrangian mesh-less finite mass (MFM) method.

2.1 Sub-grid physical processes included

To model the main physical processes responsible for galaxy formation and evolution, we employ the following sub-grid prescriptions.

- The metal chemical network and cooling/heating processes from Capelo et al. (2018), modelled via KROME (Grassi et al. 2014), that included non-equilibrium chemistry for hydrogen and helium species, and the six most relevant metal species responsible for the cooling in the ISM (Richings et al. 2014; Bovino et al. 2016) ($C, C^+, O, O^+, Si, Si^+, Si^{++}$). Compared to Capelo et al. (2018), we improved our chemical network by including three-body reactions involving H_2 (Glover & Abel 2008; Forrey 2013), H_2^+ collisional dissociation by H, and H^- collisional detachment by He (Glover & Savin 2009) for completeness. As in Lupi et al. (2018) and Lupi

¹ This value depends on the collisional partner.

(2019), we also include a clumping factor $C_\rho = 1 + b^2 \mathcal{M}^2$ in the H_2 formation rate on dust, where \mathcal{M} is the Mach number and $b = 0.4$ is a parameter accounting for the ratio between solenoidal and compressive modes (Federrath & Klessen 2012).

- A stochastic SF prescription that converts gas particles into stellar particles, where the SFR density is defined as

$$\dot{\rho}_{\text{SF}} = \varepsilon \frac{\rho_g}{t_{\text{ff}}}, \quad (1)$$

with ρ_g the local gas density, $t_{\text{ff}} = \sqrt{3\pi/(32G\rho_g)}$ the free-fall time, G the gravitational constant, and ε the SF efficiency parameter, defined as (Padoan et al. 2012)

$$\varepsilon = \varepsilon_\star \exp\left(-1.6 \frac{t_{\text{ff}}}{t_{\text{dyn}}}\right) \quad (2)$$

where $\varepsilon_\star = 0.9$ is the local SF efficiency (Semenov et al. 2016), $t_{\text{dyn}} = L/(2\sigma_{\text{eff}})$ is the dynamical time of the star-forming cloud, and L is the cloud size.² As was the case in Lupi et al. (2018), we employ a very low SF density threshold $\rho_g/m_H = 1 \text{ cm}^{-3}$ to avoid wasting time computing the SF rate in low-density, unbound regions that are never expected to form stars.

- Stellar radiation is implemented as in model *b* of Lupi et al. (2018), that showed the best agreement with on-the-fly radiative transfer calculations. With respect to Lupi et al. (2018), here we update the shielding calculation around the gas cell with the best local approximation by Safranek-Shrader et al. (2017), where the gas temperature used to estimate the Jeans length is capped at 40 K. In particular, unlike several other studies, photo-electric heating is self-consistently computed from the total flux reaching the gas cell, as in Hu et al. (2017).

- Supernova feedback is based on the mechanical feedback prescription in Lupi (2019), a variation of the publicly available implementation by Hopkins et al. (2018a). As described in Geen et al. (2015), the preprocessing by stellar radiation close to the stellar sources is able to reduce the gas density before SN events. This leads to an increase of the terminal momentum for high gas densities, corresponding to $p_{\text{fin,max}} = 4.2 \times 10^5 E_{\text{SN},51}^{16/17} \tilde{Z}^{-0.14} M_\odot \text{ km s}^{-1}$, where E_{51} is the SN energy E_{SN} in units of 10^{51} ergs and $\tilde{Z} = \max\{Z/Z_\odot, 0.01\}$ with Z_\odot the solar metallicity. Here, since we cannot properly model the radiative effect within molecular clouds, we include this additional boost by rescaling the injected momentum by a factor $f_{\text{boost}} = \max\{p_{\text{fin,max}}/p_{\text{fin}}, 1\}$, where $p_{\text{fin}} = \sqrt{2E_{\text{SN}}M_{\text{cool}}}$ is the ‘standard’ terminal momentum, with M_{cool} the cooling mass from Martizzi et al. (2015).

Motivated by Semenov et al. (2018) and Lupi (2019), we also include an additional fiducial boost to the radial momentum of a factor of two.

In our model, stellar particles represent an entire stellar population following a Kroupa initial mass function (IMF; Kroupa 2001), that release mass and energy via stellar

winds and type II/Ia SN events. The type II SN and stellar wind rates have been computed via STARBURST99 (Leitherer et al. 1999), assuming that only stars with masses between 8 and 40 M_\odot can explode as type II SNe, whereas those in the range 40–100 M_\odot directly collapse into a black hole. As in Lupi (2019), SN explosions are modelled as discrete events releasing 10^{51} erg of energy and the IMF-averaged ejecta masses, respectively a total ejecta mass $M_{\text{ej}} = 10.61 \tilde{Z}^{-0.096} M_\odot$, an oxygen mass $M_{\text{Oxy}} = 1.021 M_\odot$ and an iron mass $M_{\text{iron}} = 0.106 M_\odot$. The total metal mass injected per single event, assuming solar ratio for the Oxygen and Iron groups, respectively, corresponds to $M_Z = 2.09 M_{\text{Oxy}} + 1.06 M_{\text{iron}} = 2.246 M_\odot$. For type Ia SNe, instead, we employ the delay-time distribution from Maoz et al. (2012), spanning the stellar age interval 0.1–10 Gyr, and we inject 10^{51} erg, $M_{\text{ej}} = 1.4 M_\odot$, $M_{\text{Oxy}} = 0.14 M_\odot$, and $M_{\text{iron}} = 0.63 M_\odot$, with $M_Z = 0.9604 M_\odot$. The STARBURST99 rates for type II SNe can be well modelled by a single power-law defined as

$$\frac{\dot{N}_{\text{SN}}}{\text{Myr}^{-1} M_\odot^{-1}} = 6.8 \times 10^{-3} (t_{\text{Myr}}/t_{\text{max,Myr}})^{-0.648} / t_{\text{max,Myr}}, \quad (3)$$

for $t_{\text{min,Myr}} < t_{\text{Myr}} < t_{\text{max,Myr}}$, where t_{Myr} is the stellar population age in Myr, $t_{\text{min,Myr}} = 5.09$ is the typical lifetime of an 40 M_\odot star and $t_{\text{max,Myr}} = 38.1$ is the typical lifetime of a 8 M_\odot star. For type Ia SNe, the rate can be defined as

$$\frac{\dot{N}_{\text{SNIa}}}{\text{Myr}^{-1} M_\odot^{-1}} = 2.82 \times 10^{-4} t_{\text{Myr}}^{-1} \quad (4)$$

- Winds are implemented by distributing the wind mass and the wind energy in thermal form only, assuming a continuous damping taken from the STARBURST99 rates, that can be fitted as

$$\frac{\dot{M}_w}{\text{Myr}^{-1}} = \begin{cases} 1.9 \times 10^{-3} + 6.5 \times 10^{-4} t_{\text{Myr}} & 0.0 \leq t_{\text{Myr}} < 2.7 \\ 2.58 \times 10^{-2} & 2.7 \leq t_{\text{Myr}} < 3.3 \\ 2.58 \times 10^{-2} m_x^{(\log t_{\text{Myr}} - 0.52)/1.48} & 3.3 \leq t_{\text{Myr}} < t_x \\ 4 \times 10^{-3} m_x^{\log(t_{\text{Myr}}/t_x)/\log(25/t_x)} + 2.58 \times 10^{-3} m_x^{(\log t_{\text{Myr}} - 0.52)/1.48} & t_x < t_{\text{Myr}} < 100 \\ 5 \times 10^{-4} (t_{\text{Myr}}/100)^{-1.24} & t_{\text{Myr}} > 100 \end{cases} \quad (5)$$

with $m_x = 1.94 \times 10^{-3}$ and $t_x = 8.7 \min\{1, (0.5 + \tilde{Z}/2)^{0.4}\}$ for the mass and

$$\frac{\dot{E}_w}{L_\odot M_\odot^{-1}} = \begin{cases} 2.32 & 0.0 \leq t_{\text{Myr}} < 2.7 \\ 4.83 & 2.7 \leq t_{\text{Myr}} < 3.3 \\ 4.83 f_x^{(\log t_{\text{Myr}} - 0.54)/0.6} & 3.3 \leq t_{\text{Myr}} < 100 \\ 4.1 \times 10^{-5} (t_{\text{Myr}}/100)^{-1.24} & t_{\text{Myr}} > 100 \end{cases} \quad (6)$$

where $f_x = 1.23 \times 10^{-3}$. We note that the wind power for old stars ($t_{\text{Myr}} > 100$, producing slow winds) is simply computed as $\dot{E} = 0.5 \dot{M}_w v_{\text{eff}}^2$, with $v_{\text{eff}} = 30 \text{ km s}^{-1}$. While the metallicity dependence for old stars is very weak, for young stars we rescale the rates according to the stellar population metallicity as $\dot{M}_{w,Z} = \dot{M}_w \tilde{Z}^{0.8}$ and $\dot{E}_{w,Z} = \dot{E}_w \tilde{Z}^{1.06}$ if $t_{\text{Myr}} < 2.7$, and as $\dot{M}_{w,Z} = \dot{M}_w \min\{1, \tilde{Z}^{0.8}\}$ and $\dot{E}_{w,Z} = \dot{E}_w \min\{1, \tilde{Z}^{1.06}\}$ if $2.7 \leq t_{\text{Myr}} < t_{\text{max,Myr}}$.

During a Hubble time, the ensemble of stellar feedback prescriptions results in a mass recycling of about 40 per

² As in Lupi et al. (2018) and Lupi (2019), $L \approx 0.5h$ is the particle grid-equivalent size, with h the particle smoothing length, $\sigma_{\text{eff}} \equiv L \sqrt{\|\nabla \otimes \mathbf{v}\|^2 + (c_s/L)^2}$ is the total support against gravitational collapse, with $\nabla \otimes \mathbf{v}$ the velocity gradient in the cloud and c_s the sound speed.

Table 1. Main properties of our simulated galaxies at their final redshift. The first column is the halo mass, the second and the third are the stellar mass and the SFR, the fourth is the half-mass radius obtained from the 2D maps (first value) or from the 3D distribution (second value), the fifth the stellar metallicity, and the sixth the total [CII] luminosity.

M_{halo} ($10^9 M_{\odot}$)	M_{star} ($10^9 M_{\odot}$)	SFR ($M_{\odot} \text{ yr}^{-1}$)	R_{50} (kpc)	Z_{star} (Z_{\odot})	L_{CII} ($10^5 L_{\odot}$)
38.2	0.24	4.4×10^{-3}	1.2/1.4	0.27	0.20
70.8	1.08	8.2×10^{-2}	1.5/1.7	0.41	4.94

cent (see [Kim et al. 2014](#), and references therein). In order to resolve single SN events in our simulations, we also add a time-step limiter for stellar particles (see [Lupi 2019](#) for details).

2.2 Initial conditions

The initial conditions consist of two high-resolution regions, around halos with $M_{\text{halo}} \sim 4 \times 10^{10} M_{\odot}$ and $M_{\text{halo}} \sim 10^{11} M_{\odot}$ at $z = 0$, H1 and H2 hereafter, in a box of 10 Mpc h^{-1} co-moving. We generated the initial conditions with MUSIC ([Hahn & Abel 2013](#)), assuming the most recent cosmological parameter estimates from PLANCK ([Planck Collaboration et al. 2018](#)), where $\Omega_{\text{m}} = 0.3119$, $\Omega_{\Lambda} = 0.6881$, $\Omega_{\text{b}} = 0.04669$, and $H_0 = 67.66 \text{ km s}^{-1} \text{ Mpc}^{-1}$. We first ran a coarse level dark-matter only simulation (256^3) and selected the two haloes in the desired mass range, by enforcing a strong isolation criterion, i.e. no haloes more massive than half the target mass were present within a sphere of $3R_{\text{vir}}$, with R_{vir} the halo virial radius.

To identify the haloes in the simulation we employed AMIGA HALO FINDER ([Knollmann & Knebe 2009](#), AHF hereafter). To refine the target region, we followed the procedure described by [Fiacconi et al. \(2017\)](#) and [Lupi et al. \(2019\)](#) by recursively selecting and tracing back in time all the particles within $3R_{\text{vir}}$ at $z = 0$.

The mass resolution in the high-resolution region is $\sim 1.2 \times 10^4 M_{\odot}$ for dark matter particles and $\sim 2.2 \times 10^3 M_{\odot}$ for gas and star particles. The gravitational softening for dark matter and stars in the high-resolution region is fixed at 60 and 7 pc h^{-1} , respectively, whereas we employ fully adaptive gravitational softening for the gas, which ensures both hydrodynamics and gravity are computed assuming the same mass distribution within the kernel. The minimum allowed softening, which sets the maximum resolution of the simulation, is set to 0.5 pc h^{-1} , corresponding to an inter-particle spacing of ~ 1 pc.

3 RESULTS

Here, we present our results, focusing first on the galaxy properties at the final redshift of the runs, i.e. $z = 0$ for H1 and $z = 0.4$ for H2, and later on the redshift evolution. For all the analysis, we only consider particles within a sphere of $0.2R_{\text{vir}}$, to exclude any possible satellites around the target galaxies. The main properties are reported in Table 1.

In Fig. 1, we show the stellar-to-halo mass relation for our dwarf galaxies (red stars), compared with observational data from [Beasley et al. \(2016\)](#), where the halo mass is

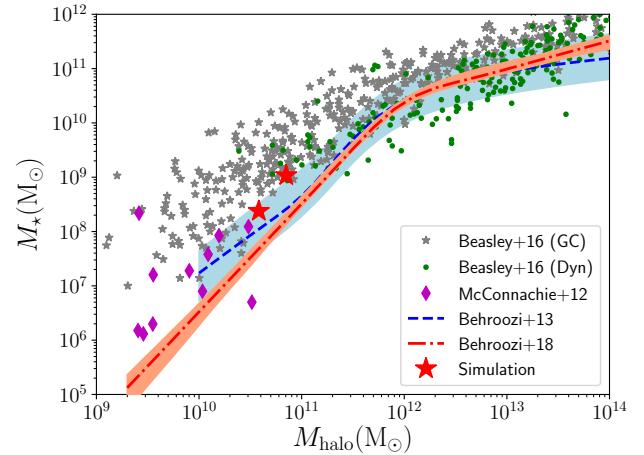


Figure 1. Stellar-to-halo mass relation in the simulations, compared with observations and semi-empirical models. The grey stars correspond to the halo mass from globular cluster measurement from [Beasley et al. \(2016\)](#), the green dots to their dynamical mass estimates, and the magenta diamonds to the dwarf galaxies in the Local Group by [McConnachie \(2012\)](#). The blue dashed line is the model by [Behroozi et al. \(2013\)](#) and the red one is the updated model from [Behroozi et al. \(2018\)](#), both at $z = 0$, with the light-blue and orange shaded areas representing the 3σ uncertainty in the models. Our simulations, shown as red stars, are in good agreement with the data, well within the uncertainties.

estimated from globular cluster counting (grey stars) and dynamical measure (green dots), Local Group dwarf galaxies from [McConnachie \(2012\)](#), and the semi-empirical models by [Behroozi et al. \(2013\)](#) and [Behroozi et al. \(2018\)](#), reported as a blue dashed line and a red dot-dashed line, respectively. The shaded areas correspond to 3σ uncertainty in the models. Our galaxies are in good agreement with both observations and theoretical models, lying within the scatter of the data.

In Fig. 2, we show the half-mass radius of the two galaxies as a function of the stellar mass, compared with the dwarf spheroidal galaxies from [Forbes et al. \(2011\)](#), shown as green squares, and the results from the 3D+HST+CANDELS survey ([van der Wel et al. 2014](#)), reported through the best-fit to late type (black dashed line) and early type (black dotted line) galaxies at $0.25 < z < 0.75$. The cyan and grey dashed areas correspond to 1σ and 3σ uncertainty, respectively. Our simulations are reported as blue stars (computing the size in 3D radial bins) and red stars (computing the size from the 2D face-on projection), and exhibit a very good agreement with the observational data, in particular with the dwarf spheroidals. In Fig. 3, we report the stellar mass–metallicity relation, compared with the local dwarfs by [Kirby et al. \(2013\)](#), orange squares, the CALIFA survey from [González Delgado et al. \(2014\)](#), cyan dots, and the median from [Galazzi et al. \(2005\)](#), shown as a magenta line, with the grey shaded area corresponding to the 16th and 84th percentiles of the distribution. Because of the different assumptions on the solar metallicities when deriving these relations, that are $Z_{\odot} = 0.02$ [Anders & Grevesse \(1989\)](#) or $Z_{\odot} = 0.013$ [Asplund et al. 2009](#), we show the expected metallicity by employing both definitions, respectively as blue and red stars. Independ-

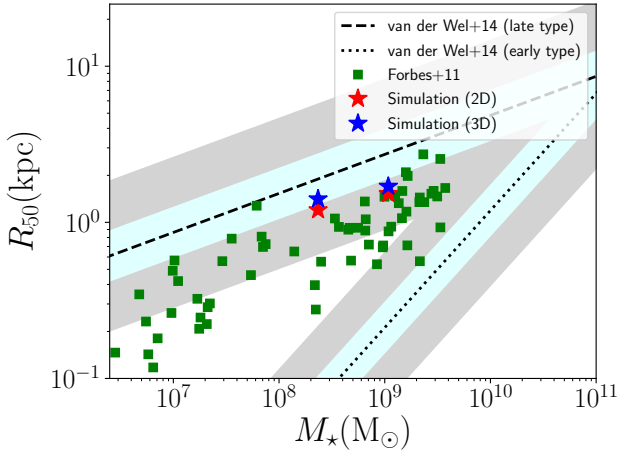


Figure 2. Stellar mass-size relation in the simulations, compared with observations from the 3D+HST+CANDELS survey for $0.25 < z < 0.75$ (black dashed lines and corresponding shaded areas tracing 1- and 3σ uncertainties van der Wel et al. 2014) and the dwarf spheroidal galaxies from Forbes et al. (2011), shown as green squares. Our simulations agree very well with the data, almost exactly following the trend observed for dwarf spheroidal galaxies.

dent of the definition for Z_\odot , our results are in very good agreement with local dwarfs, and are very close to the median by Gallazzi et al. (2005), despite the stellar mass in the H1 run is just outside the available data interval.

3.1 SF history and the Schmidt–Kennicutt relation

Here, we discuss the SF history of the galaxies and we compare our results with the spatially-resolved local correlation between the gas and the SFR surface densities, the so-called Schmidt–Kennicutt relation (KS hereafter; Schmidt 1959; Kennicutt 1998). In Fig. 4, we report the SF history of the target galaxies as a function of time/redshift. In H1, stars begin to form already at $z > 6$, with a SFR of about $0.03 \text{ M}_\odot \text{ yr}^{-1}$ that lasts until $z \sim 2$. These ‘high’ SFRs are responsible for most of the SF occurring in the galaxy, that almost reaches its final mass by $z = 2$. At later times, instead, the typically lower gas densities, together with the radiative heating from the uniform UV background and the local sources in the galaxy result in the suppression of the SFR at about $\dot{M}_{\text{star}} \sim 10^{-3} \text{ M}_\odot \text{ yr}^{-1}$. In H2, instead, the SFR does not vary significantly with time, only slightly declining from the peak of $\sim 0.3 \text{ M}_\odot \text{ yr}^{-1}$ at $z \sim 5$ to about $0.1 \text{ M}_\odot \text{ yr}^{-1}$. This explains the steady increase in stellar mass, that reaches 10^9 M_\odot by $z = 0.4$. In this second case, less than half of the mass is assembled before $z = 2$.

Now, in Fig. 5 we show the KS relation in total gas ($\text{H}+\text{H}_2$), computed in concentric annuli 500 pc wide, for $z = 2$ (red dots), $z = 1$ (blue dots), $z = 0.5$ (green dots), and $z = 0$ (cyan dots). The SFR is estimated from the far UV luminosity L_{FUV} of the stellar particles in the simulation, assuming the calibration by Salim et al. (2007), i.e.

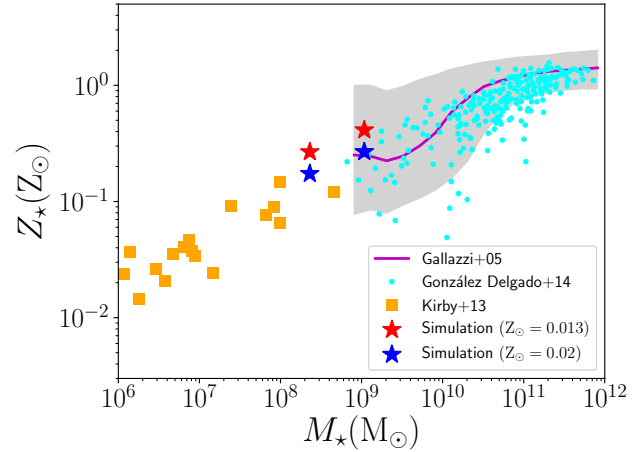


Figure 3. Stellar mass-metallicity relation in the simulations, compared with observations of local dwarfs (Kirby et al. 2013, orange squares), normal galaxies of the CALIFA survey (González Delgado et al. 2014, cyan dots), and those by Gallazzi et al. (2005), for which we show the median profile as a magenta solid line and the uncertainty within the 16th and 84th percentile as a grey shaded area. Our simulation results are shown as stars, assuming different definitions for the solar metallicity, i.e. red for Asplund et al. (2009) and blue for Anders & Grevesse (1989). Our results are in very good agreement with local dwarfs, and also consistent with the low-mass end of the CALIFA survey.

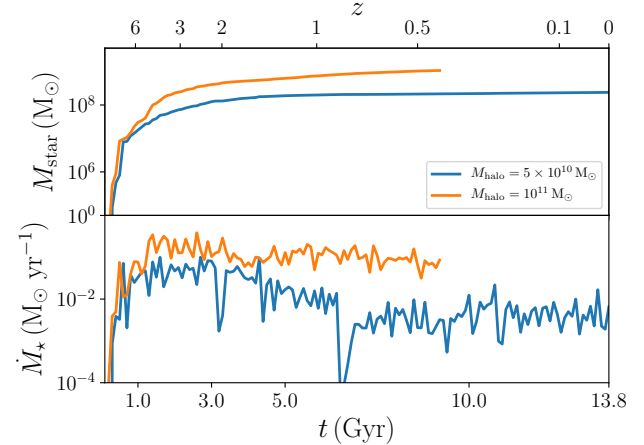


Figure 4. SF history of the target galaxies in bins of 100 Myr. The top panel shows the stellar mass as a function of time, whereas the bottom panel shows the SFR. In H1, most of the stellar mass is built up in the first 3 Gyr (above $z = 2$), when the average SFR exceeds $0.01 \text{ M}_\odot \text{ yr}^{-1}$, whereas H2 assembles less than half its mass by this time. At later times, instead, the lower gas densities, combined with the stronger radiative heating (UV background and local source) result in a suppression of the SFR at about $\dot{M}_{\text{star}} \sim 10^{-3} \text{ M}_\odot \text{ yr}^{-1}$ for H1, while H2 continues to form stars at a steady pace of about $0.1 \text{ M}_\odot \text{ yr}^{-1}$.

$\dot{M}_{\text{star}} = 0.6 \times 10^{-28} L_{\text{FUV}}$.³ The filled contours correspond to the observations by Bigiel et al. (2008) (green color-scale) and Bigiel et al. (2010) (red color-scale), where the different colours correspond to 2, 5, and 10 points per bin. Compared to Lupi (2019), here the agreement between the simulation and observations is very good.

In dwarf galaxies, SF mostly occurs in the HI-dominated regime ($\Sigma_{\text{H+H}_2} \lesssim 10 \text{ M}_\odot \text{pc}^{-2}$, where H₂ is strongly subdominant (e.g. Hu et al. 2017), hence the molecular KS correlation is not expected to always hold, especially for very-small galaxies. Indeed, for H1, most of our data lies below the transition surface density, whereas for H2 more data are found above this threshold.

We report the molecular KS relation in Fig. 6, comparing our simulations with observations by Bigiel et al. (2008) (green contours) and Schrubba et al. (2011) (magenta contours). In H1, we observe that only a few regions exhibit an agreement with this correlation, whereas the others show a deficit in H₂, as expected. This deficit is due to the strong impact of SNe onto the dense gas, that is quickly evacuated, on time-scales much shorter than those traced by the far UV emission. In H2, instead, where SNe start to become less effective, most of the examined patches lie within the observational scatter, with only a few of them lying above (due to the still strong impact of SNe) or even below (where the formed H₂ has not been converted yet into stars, likely because of the moderately lower densities and stronger turbulent support). In general, our simulations show a good agreement with observations, especially at low redshift ($z \leq 0.4$), when most of the patches lie at the centre of the observational contours.

3.2 The [CII]–SFR correlation

After having shown that our galaxy agrees well with observational constraints, we now focus on the [CII] emission from the galaxy, in the aim at assessing whether we can reproduce the expected correlation by De Looze et al. (2014), and its evolution with metallicity. Thanks to the chemical network we have in our simulations, we can directly follow the abundances of different elements during the cosmic evolution. An example of the chemical species surface density is shown in Fig. 7 for our H2 galaxy at $z = 0.4$. The left-most panel corresponds to the total gas surface density, the middle-left one to the C⁺ one, the middle-right one to the O one, and the rightmost to the SFR surface density derived from the FUV emission, respectively. We can clearly see that on one hand O appears more abundant in dense and cold regions compared to C⁺, that instead more effectively recombines to neutral C at high densities, suppressing the expected [CII] emission. On the other hand, O can remain in its neutral form also at intermediate densities, hence partially contributing to the total OI emission, where we expect most of the [CII] emission being produced. Consistently with this distribution, star-forming gas in the galaxy appears concentrated in the densest regions, likely corresponding to molecular clouds. By comparing the relative abundance of C⁺ and O, the latter appears to be a better tracer of SF

compared to the former. However, a proper comparison cannot be made on the basis of abundances alone, but requires the estimation of the effective FIR lines emissivity, that is strongly dependent on the thermodynamic state of the gas and the relative abundance of colliders able to excite the line transition (see Grassi et al. 2014, for details). By using KROME, we can estimate the emission of the [CII] and the [OI]₆₃ lines from our chemical network, and directly compare them with observations. Here we focus on the [CII] only, and defer the reader to Appendix A for a similar analysis applied to the [OI]₆₃ case. In Fig. 8, we compare our simulations (red dots) with the spatially-resolved correlation by De Looze et al. (2014) for dwarf galaxies, shown as a black solid line (best-fit) and as blue dots (data), and the best-fit for normal, nearby galaxies from the KINGFISH sample by Herrera-Camus et al. (2015), shown as a blue dashed line (with the 3σ uncertainties identified by the grey and cyan shaded areas, respectively). The simulation data is binned in square patches 500 pc wide, with the SFR derived from the far UV luminosity and the [CII] luminosity from the corresponding cooling rate estimated by KROME at 158 μm . Our simulation shows a good agreement with the correlations by De Looze et al. (2014) and Herrera-Camus et al. (2015). The combined scatter of the two runs is slightly larger than that observed, but observations in this luminosity range are still missing, and future observations with higher sensitivity will be crucial to improve the fit and validate/confute our results.

While a spatially-resolved correlation can be obtained for local galaxies with high-resolution observations, at high redshift this is not achievable anymore, and the integrated correlation is employed instead. Now, we investigate the metallicity evolution of the integrated correlation, by computing the ratio between the total [CII] luminosity $L_{\text{[CII]}}$ and the SFR \dot{M}_{star} . Since we follow a single galaxy only, the metallicity evolution directly follows from the redshift evolution, and we cannot disentangle any distinct effect among the two. According to Vallini et al. (2015), at $z \gtrsim 4$, the higher CMB temperature goes into equilibrium with the spin temperature of the transition powering the [CII] line, and the stronger UV pumping changes the state populations. This results in a suppression of the [CII] luminosity. At lower redshift, this effect disappears, and the [CII]–SFR correlations loses any intrinsic dependence on redshift. For this reason, we can safely assume here that the only evolution of the correlation expected in our simulations is due to the metallicity evolution of the galaxy. In Fig. 9, we show the ratio at different metallicities for the two galaxies, compared with the predictions by Vallini et al. (2015) and the best-fits from De Looze et al. (2014) for the DGS galaxies (red dashed line) and from Herrera-Camus et al. (2018) for galaxies with normal SF efficiency (SFE; blue dotted line). The shaded areas correspond to the scatter in the relations, i.e. 0.32 and 0.26 dex, respectively. The two runs, shown as black stars (H1) and squares (H2), exhibit a clear evolution with metallicity, with a surprisingly good agreement with the theoretical model by Vallini et al. (2015), and only approaching the De Looze et al. (2014) and Herrera-Camus et al. (2018) data at $z = 0$ and $Z \sim 0.3 - 0.5 Z_\odot$.

Unfortunately, due to the scatter in the observed [CII]–SFR correlation, the evolutionary trend we observed in the simulation can easily remain hidden within the uncertainty.

³ We also computed the SFR directly from stellar particles in the simulations, finding consistent results.

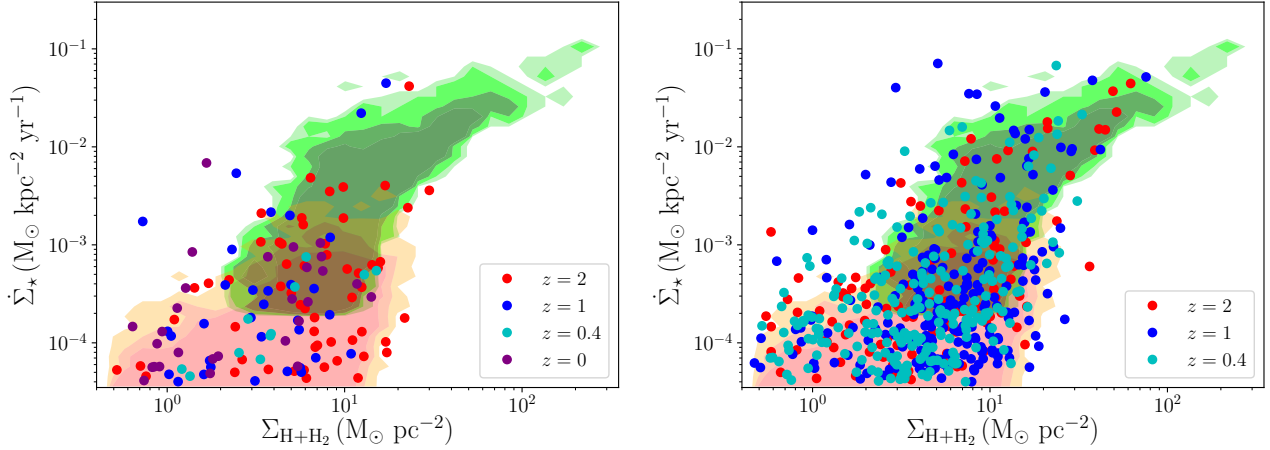


Figure 5. KS relation in total gas at $z = 0$ for the target galaxies (H1 on the left and H2 on the right) in our simulations (filled dots) at $z = 2, 1, 0.4$, and 0 (for H1 only), compared with the observations by Bigiel et al. (2008) (green contours) and Bigiel et al. (2010) (red contours). The increased momentum injected by SNe is able to heat the gas up more effectively, resulting in a good agreement between simulations and observations.

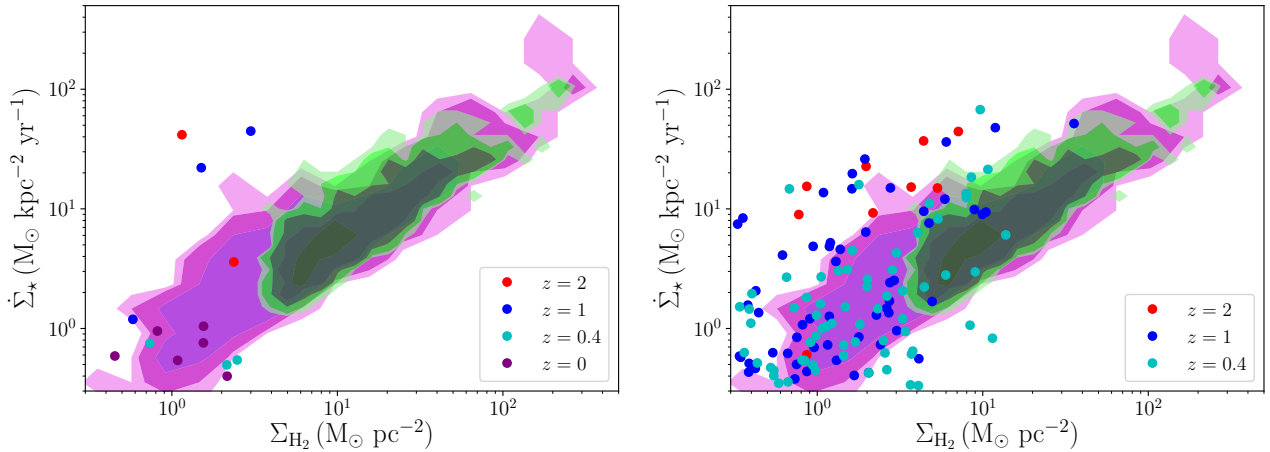


Figure 6. KS relation in molecular gas at $z = 0$ for the target galaxies in our simulations (filled dots) at $z = 2, 1, 0.4$, and 0 (for H1 only), compared with the observations by Bigiel et al. (2008) (green contours) and Schrubba et al. (2011) (magenta contours). Despite the few points, the simulation is in reasonable agreement with the observations, except for three points at higher redshift that lie above the correlation (due to SNe quickly evacuating the star-forming high-density gas).

Indeed, if we consider the 3σ scatter in the sample, with $\sigma \approx 0.3$, all our data points fall within the uncertainty range.

3.3 The [CII] emitting gas distribution

In Fig. 10, we show the normalised cumulative [CII] emission from our galaxies as a function of $Z(z)$, and compare it with isolated dwarf simulations by Hu et al. (2017). Similarly to Hu et al. (2017), our results suggest that a significant fraction of the total [CII] emission comes from cold neutral gas at low and intermediate densities, and only a small fraction from the high density typical of photo-dissociation regions (PDRs). This is also consistent with the observational results by Fahrion et al. (2017), where they observe 46 per cent of the [CII] emission produced in the neutral medium (where the neutral hydrogen emission dominates), and only 9 per cent coming from the cold neutral medium. However,

we notice that, unlike Hu et al. (2017), the cosmological evolution we considered here results in large variations of the emission distribution, that reflect the evolution of the gas in the galaxies with metallicity. In particular, we can follow our target galaxies throughout the entire cosmic history, self-consistently modelling gas inflows from large scales and galaxy mergers, that affect in a non-trivial way the ISM evolution. By looking at the normalised cumulative emissivity $L_{\text{[CII]}}/M_{\text{gas}}$, we notice a completely different trend, where most of the emissivity is produced by dense gas, that accounts for a small fraction of the mass only. This suggests that the dense gas, that is typically closer to stellar sources and for which collisions are more frequent, is more effectively excited than its low-density and warmer counterpart, producing a stronger emissivity, but also that its small contribution to the total mass suppresses the total luminosity produced, which is instead dominated by the volume-

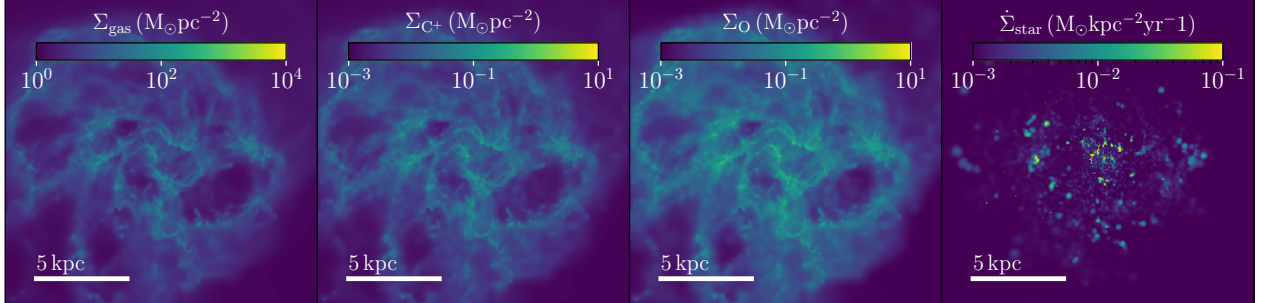


Figure 7. Surface density maps of total gas (leftmost panel), C^+ (middle-left panel), O (middle-right panel), and SFR (rightmost panel) for our H2 run at $z = 0.4$. Although strongly perturbed by SN explosions, the galaxy clearly exhibits a disk-like distribution, with C^+ and especially O showing a stronger contrast relative to the total gas in dense regions, i.e. the regions that also produce the bulk of the emissivity of the galaxy. Consistently, in the rightmost panel SF is observed mainly in these dense regions, that likely correspond to molecular clouds.

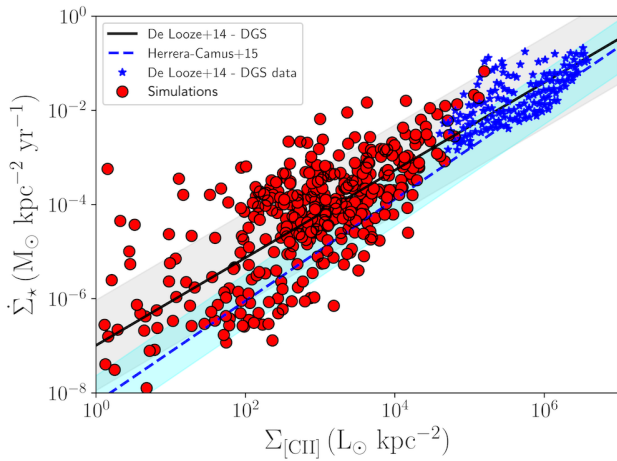


Figure 8. Spatially-resolved [CII]–SFR correlation in the simulations (red dots), compared with the best-fits for the DGS galaxies by [De Looze et al. \(2014\)](#), shown as a black solid line, and for the KINGFISH sample by [Herrera-Camus et al. \(2015\)](#), shown as a blue dashed line, where the grey and cyan shaded areas corresponds to the 3σ uncertainties. The DGS data is shown as purple stars. Our simulation data, binned in square patches 500 pc wide, exhibits a good agreement with both correlations by [De Looze et al. \(2014\)](#) and [Herrera-Camus et al. \(2015\)](#), despite having a large scatter.

filling lower density gas. These trends are clearly visible in both our runs, but with some differences. While in H1 both the emission and emissivity distributions evolve significantly with metallicity, shifting to lower density, in H2 the variation is modest, with the two profiles biased toward moderately higher densities. The origin of this difference is two-folds. First, as the metallicity increases, metal cooling becomes more efficient, hence [CII] emission becomes stronger, even at lower densities, as can be easily seen in the top panel for H1 (and also in H2, despite to a smaller degree). Secondly,

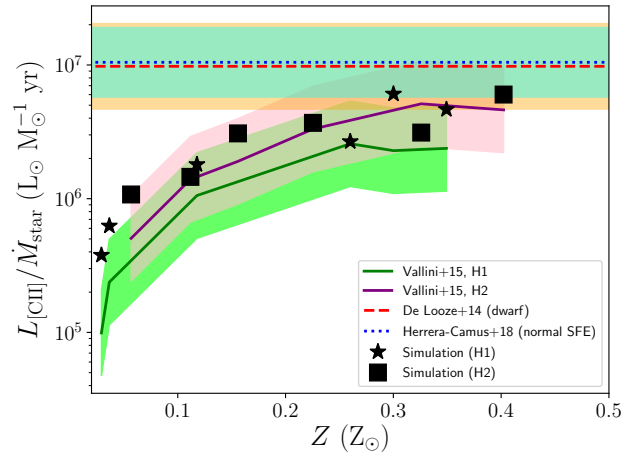


Figure 9. Redshift evolution of the ratio $L_{[CII]}/\dot{M}_{\text{star}}$ with redshift, compared with the model predictions by [Vallini et al. \(2015\)](#), green solid line), the observed correlation by [De Looze et al. \(2014\)](#) for the DGS sample (red dashed line), and the correlation by [Herrera-Camus et al. \(2018\)](#) for galaxies with normal SFE (blue dotted line). The shaded areas correspond to the 1σ uncertainties, i.e. 0.32 and 0.26 dex, respectively. Our simulations are reported as black stars (H1) and squares (H2), as a function of the average gas metallicity in the galaxy during its redshift evolution. The results suggest a clear metallicity evolution for the correlation, in agreement with [Vallini et al. \(2015\)](#).

a more massive halo (like H2) is able to retain dense gas after SN events, whereas smaller haloes like H1 see their dense gas completely evacuated after each SN event. Our results are also consistent with those obtained by [Franeck et al. \(2018\)](#) on synthetic maps of molecular clouds, further reinforcing our conclusions.

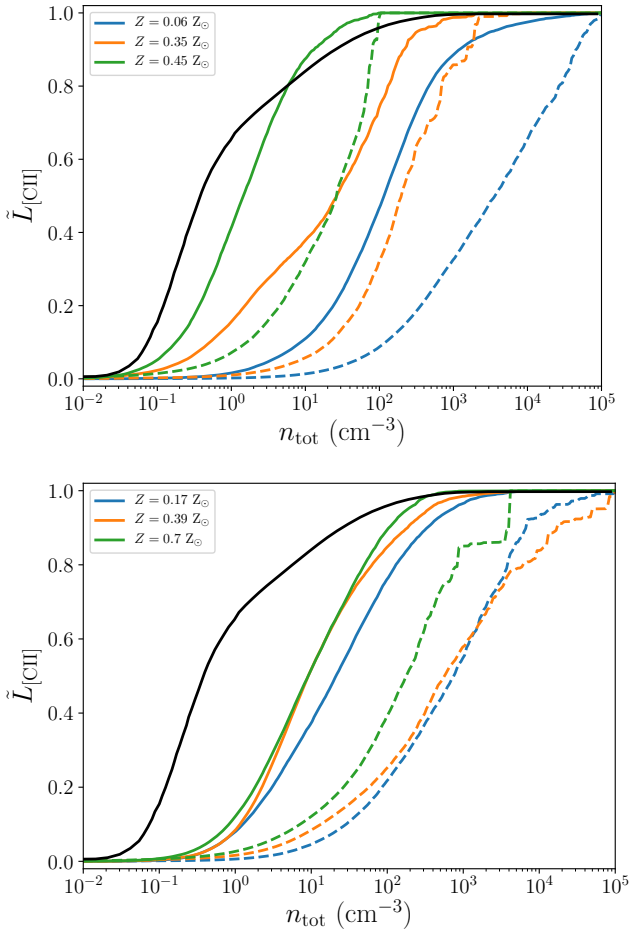


Figure 10. Redshift evolution of the normalised cumulative [CII] emission as a function of gas number density for H1 (top panel) and H2 (bottom panel), shown as the coloured solid lines, for different metallicities. The black line corresponds to the fiducial model by Hu et al. (2017). The dashed lines represent instead the normalised cumulative emissivity $L_{\text{[CII]}}/M_{\text{gas}}$. Our results for H1 look vaguely similar to those by Hu et al. (2017), with a significant fraction of the [CII] emission coming from low- and intermediate-density gas, the so-called cold neutral medium, but slightly shifted toward higher densities. For H2, instead, the curves shift toward higher densities, as expected for more massive galaxies where dense gas can survive for longer times before being evacuated by SNe. From the emissivity curves, instead, we see in both panels that the largest contribution comes from dense and colder gas, that accounts for most of the mass, but has a smaller volume filling factor.

4 CONCLUSIONS

We have presented here two zoom-in cosmological simulations of dwarf galaxies including a self-consistent non-equilibrium metal network (Capelo et al. 2018). Compared to previous studies by Lupi (2019) and Lupi (2019), we have improved the sub-grid models employed, that now include young stellar winds and an updated SF prescription independent of the Mach number. Thanks to the state-of-the-art sub-grid modelling employed, we have been able to well reproduce the main observed properties of local dwarf galaxies. The very high resolution achieved and the ability to

directly follow the C^+ abundance in the simulation have enabled us to accurately investigate the emergence of the correlation between the [CII] emission and the star formation rate, both spatially resolved and integrated over the entire galaxy, throughout the entire cosmic evolution of the galaxy. Our findings can be summarised as following:

- (i) the local correlations observed by De Looze et al. (2014) and Herrera-Camus et al. (2015) are very well recovered in our simulation, both in slope and normalisation. Since our data is outside the currently observed range, higher resolution and deeper observations are necessary to assess the accuracy of our model in reproducing the [CII]–SFR relation;
- (ii) at lower metallicity, the correlation seems to evolve in agreement with the predictions by Vallini et al. (2015), but this evolution is hard to find in observations because of the large scatter in the De Looze et al. (2014) data (~ 0.42 dex);
- (iii) the [CII] emission distribution in dwarfs suggests that most of the emission comes from the CNM ($n_{\text{gas}} \lesssim 100 \text{ cm}^{-3}$), and only a small fraction from the higher densities typical of PDRs, in agreement with the simulation results by Hu et al. (2017) and Franeck et al. (2018), and SOFIA observations by Fahrion et al. (2017). This is due to the large volume filling factor of the low-density gas, as demonstrated by the normalised cumulative emissivity, that is dominated by the cold and dense gas (likely in PDRs) where most of the mass is confined but the occupied volume is small.

Of course, the intrinsic limitations of this study, like the missing additional processes like HII regions around stars (Hu et al. 2017; Hopkins et al. 2018b), cosmic rays, etc., the inability to properly resolve the PDRs, and the missing galaxy population statistics (we only considered two galaxies due to the computational cost of the runs), does not allow us to give a more conclusive answer on the metallicity dependence of the [CII]–SFR correlation. Nevertheless, the agreement found in the evolution of two completely different galaxies is a hint that our conclusion could be real. This study is only meant to represent a first attempt to address this important question and the related consequences about the significance of the [CII] as a SFR tracer, and a more detailed exploration is definitely necessary.

ACKNOWLEDGEMENTS

We thank the anonymous referee for useful comments that helped improving the quality of the manuscript. The authors thank Rodrigo Herrera-Camus and Livia Vallini for fruitful discussions. AL acknowledges support from the European Research Council No. 740120 ‘INTERSTELLAR’. SB is financially supported by Fondecyt Iniciación (project code 11170268) and Conicyt Apoyo a la Formación de Redes Internacionales project number REDI170093. SB also acknowledges support by BASAL Centro de Astrofísica y Tecnologías Afines (CATA) AFB-17002. The authors acknowledge the UdeC Kultrun Astronomy Hybrid Cluster (projects Conicyt Programa de Astronomía FondoQuimal QUIMAL170001, Conicyt PIA ACT172033, and Fondecyt Iniciación 11170268) for providing HPC resources that have contributed to the research results reported in this paper.

REFERENCES

- Anders E., Grevesse N., 1989, *Geochim. Cosmochim. Acta*, **53**, 197
- Asplund M., Grevesse N., Sauval A. J., Scott P., 2009, *ARA&A*, **47**, 481
- Beasley M. A., Romanowsky A. J., Pota V., Navarro I. M., Martinez Delgado D., Neyer F., Deich A. L., 2016, *ApJ*, **819**, L20
- Behroozi P. S., Wechsler R. H., Wu H.-Y., 2013, *ApJ*, **762**, 109
- Behroozi P., Wechsler R., Hearin A., Conroy C., 2018, arXiv e-prints, p. [arXiv:1806.07893](https://arxiv.org/abs/1806.07893)
- Bigiel F., Leroy A., Walter F., Brinks E., de Blok W. J. G., Madore B., Thornley M. D., 2008, *AJ*, **136**, 2846
- Bigiel F., Leroy A., Walter F., Blitz L., Brinks E., de Blok W. J. G., Madore B., 2010, *AJ*, **140**, 1194
- Bovino S., Grassi T., Capelo P. R., Schleicher D. R. G., Banerjee R., 2016, *A&A*, **590**, A15
- Brauher J. R., Dale D. A., Helou G., 2008, *ApJS*, **178**, 280
- Capak P. L., et al., 2015, *Nature*, **522**, 455
- Capelo P. R., Bovino S., Lupi A., Schleicher D. R. G., Grassi T., 2018, *MNRAS*, **475**, 3283
- Cormier D., et al., 2015, *A&A*, **578**, A53
- Cowie L. L., Songaila A., Hu E. M., Cohen J. G., 1996, *AJ*, **112**, 839
- De Looze I., Baes M., Bendo G. J., Cortese L., Fritz J., 2011, *MNRAS*, **416**, 2712
- De Looze I., et al., 2014, *A&A*, **568**, A62
- Fahrion K., et al., 2017, *A&A*, **599**, A9
- Federrath C., Klessen R. S., 2012, *ApJ*, **761**, 156
- Ferland G. J., et al., 2013, *Rev. Mexicana Astron. Astrofis.*, **49**, 137
- Fiacconi D., Mayer L., Madau P., Lupi A., Dotti M., Haardt F., 2017, *MNRAS*, **467**, 4080
- Forbes D. A., Spitler L. R., Graham A. W., Foster C., Hau G. K. T., Benson A., 2011, *MNRAS*, **413**, 2665
- Forrey R. C., 2013, *ApJ*, **773**, L25
- Franeck A., et al., 2018, *MNRAS*, **481**, 4277
- Gallazzi A., Charlot S., Brinchmann J., White S. D. M., Tremonti C. A., 2005, *MNRAS*, **362**, 41
- Geen S., Rosdahl J., Blaizot J., Devriendt J., Slyz A., 2015, *MNRAS*, **448**, 3248
- Glover S. C. O., Abel T., 2008, *MNRAS*, **388**, 1627
- Glover S. C. O., Savin D. W., 2009, *MNRAS*, **393**, 911
- Goldsmith P. F., Langer W. D., Pineda J. L., Velusamy T., 2012, *ApJS*, **203**, 13
- González Delgado R. M., et al., 2014, *ApJ*, **791**, L16
- Grassi T., Bovino S., Schleicher D. R. G., Prieto J., Seifried D., Simoncini E., Gianturco F. A., 2014, *MNRAS*, **439**, 2386
- Hahn O., Abel T., 2013, MUSIC: Multi-Scale Initial Conditions, Astrophysics Source Code Library (ascl:1311.011)
- Herrera-Camus R., et al., 2015, *ApJ*, **800**, 1
- Herrera-Camus R., et al., 2018, *ApJ*, **861**, 95
- Hopkins P. F., 2015, *MNRAS*, **450**, 53
- Hopkins P. F., et al., 2018a, *MNRAS*, **477**, 1578
- Hopkins P. F., et al., 2018b, *MNRAS*, **480**, 800
- Hu C.-Y., 2019, *MNRAS*, **483**, 3363
- Hu C.-Y., Naab T., Walch S., Glover S. C. O., Clark P. C., 2016, *MNRAS*, **458**, 3528
- Hu C.-Y., Naab T., Glover S. C. O., Walch S., Clark P. C., 2017, *MNRAS*, **471**, 2151
- Hunter D. A., et al., 2012, *AJ*, **144**, 134
- Israel F. P., Maloney P. R., Geis N., Herrmann F., Madden S. C., Poglitsch A., Stacey G. J., 1996, *ApJ*, **465**, 738
- Jameson K. E., et al., 2018, *ApJ*, **853**, 111
- Katz H., et al., 2019, arXiv e-prints,
- Kaufman M. J., Wolfire M. G., Hollenbach D. J., Luhman M. L., 1999, *ApJ*, **527**, 795
- Kennicutt Jr. R. C., 1998, *ApJ*, **498**, 541
- Kim J.-h., et al., 2014, *ApJS*, **210**, 14
- Kirby E. N., Cohen J. G., Guhathakurta P., Cheng L., Bullock J. S., Gallazzi A., 2013, *ApJ*, **779**, 102
- Knollmann S. R., Knebe A., 2009, *ApJS*, **182**, 608
- Kroupa P., 2001, *MNRAS*, **322**, 231
- Leitherer C., et al., 1999, *The Astrophysical Journal Supplement Series*, **123**, 3
- Leroy A. K., et al., 2011, *ApJ*, **737**, 12
- Luhman M. L., Satyapal S., Fischer J., Wolfire M. G., Sturm E., Dudley C. C., Lutz D., Genzel R., 2003, *ApJ*, **594**, 758
- Lupi A., 2019, *MNRAS*, **484**, 1687
- Lupi A., Bovino S., Capelo P. R., Volonteri M., Silk J., 2018, *MNRAS*, **474**, 2884
- Lupi A., Volonteri M., Decarli R., Bovino S., Silk J., Bergeron J., 2019, arXiv e-prints,
- Madden S. C., Poglitsch A., Geis N., Stacey G. J., Townes C. H., 1997, *ApJ*, **483**, 200
- Madden S. C., et al., 2013, *PASP*, **125**, 600
- Maiolino R., et al., 2015, *MNRAS*, **452**, 54
- Maoz D., Mannucci F., Brandt T. D., 2012, *MNRAS*, **426**, 3282
- Martizzi D., Faucher-Giguère C.-A., Quataert E., 2015, *MNRAS*, **450**, 504
- McConnachie A. W., 2012, *AJ*, **144**, 4
- Padoan P., Haugbølle T., Nordlund Å., 2012, *ApJ*, **759**, L27
- Pallottini A., Ferrara A., Bovino S., Vallini L., Gallerani S., Maiolino R., Salvadori S., 2017, *MNRAS*, **471**, 4128
- Pineda J. L., Langer W. D., Velusamy T., Goldsmith P. F., 2013, *A&A*, **554**, A103
- Planck Collaboration et al., 2018, arXiv e-prints, p. [arXiv:1807.06209](https://arxiv.org/abs/1807.06209)
- Richings A. J., Schaye J., 2016, *MNRAS*, **458**, 270
- Richings A. J., Schaye J., Oppenheimer B. D., 2014, *MNRAS*, **442**, 2780
- Safranek-Shrader C., Krumholz M. R., Kim C.-G., Ostriker E. C., Klein R. I., Li S., McKee C. F., Stone J. M., 2017, *MNRAS*, **465**, 885
- Salim S., et al., 2007, *ApJS*, **173**, 267
- Schmidt M., 1959, *ApJ*, **129**, 243
- Schruba A., et al., 2011, *AJ*, **142**, 37
- Semenov V. A., Kravtsov A. V., Gnedin N. Y., 2016, *ApJ*, **826**, 200
- Semenov V. A., Kravtsov A. V., Gnedin N. Y., 2018, *ApJ*, **861**, 4
- Smith J. D. T., et al., 2017, *ApJ*, **834**, 5
- Springel V., 2005, *MNRAS*, **364**, 1105
- Stacey G. J., Geis N., Genzel R., Lugten J. B., Poglitsch A., Sternberg A., Townes C. H., 1991, *ApJ*, **373**, 423
- Tremonti C. A., et al., 2004, *ApJ*, **613**, 898
- Vallini L., Gallerani S., Ferrara A., Pallottini A., Yue B., 2015, *ApJ*, **813**, 36
- Wolfire M. G., Hollenbach D., McKee C. F., Tielens A. G. G. M., Bakes E. L. O., 1995, *ApJ*, **443**, 152
- Wolfire M. G., McKee C. F., Hollenbach D., Tielens A. G. G. M., 2003, *ApJ*, **587**, 278
- van der Wel A., et al., 2014, *ApJ*, **788**, 28

APPENDIX A: VALIDATION OF THE CHEMICAL MODEL FOR COSMOLOGICAL SIMULATIONS: THE GALAXY MASS DEPENDENCE OF THE [CII]–SFR AND [OI]–SFR CORRELATIONS

As in Capelo et al. (2018), the chemical network employed here includes both C and O atoms, the main elements responsible for radiative cooling in the ISM below 10^4 K. In their isolated galaxy simulations, Capelo et al. (2018)

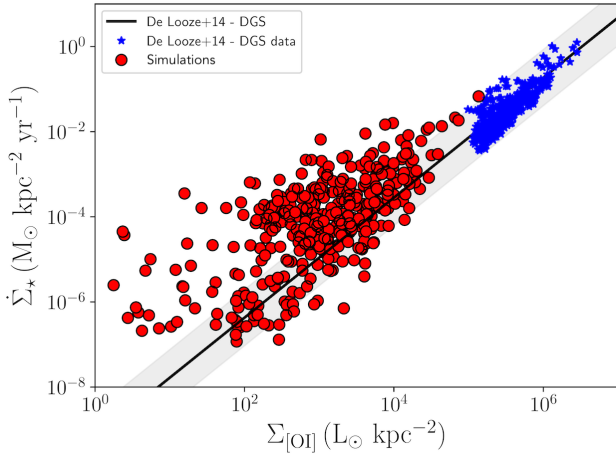


Figure A1. Spatially-resolved [OI]–SFR correlation in the simulations, compared with the best-fit by De Looze et al. (2014), shown as a black solid line, where the grey shaded area corresponds to the 3σ uncertainty. Our simulations (red dots), binned in square patches 500 pc wide, appear to be offset with respect to the observed correlation. This is likely due to the lower abundance of moderately dense regions of gas in the galaxies, consequence of the shallow potential well and the strong impact of SN feedback. In H2, where the galaxy is more massive, the data start to approach the observed correlation, although the agreement is not recovered yet.

showed that both the [CII]–SFR and the [OI]–SFR correlations could be reproduced at the same time in sub-L* galaxies with sub-solar metallicity. However, in a cosmological context, this is not necessarily guaranteed. Indeed, in our dwarf galaxy simulations, while the [CII]–SFR correlation exhibits good agreement with the extrapolation of the observed correlation, the [OI]–SFR is moderately offset (see Fig. A1). From a physical point of view, this behaviour can be explained by considering that, while [CII] is also excited in the diffuse neutral medium, the [OI] emission is dominated by denser gas closer to SF regions, which in our simulations are rare and short-lived due to SN feedback. To test this idea, and exclude a possible numerical origin of this result (due to the resolution or the sub-grid modelling), we have performed a cosmological simulation of a more massive galaxy with the same sub-grid models of the fiducial run. The initial conditions are taken from the FIRE2 simulation suite (Hopkins et al. 2018b), and correspond to a Milky Way-like halo (namely the *m12i* case). To limit the computational cost of the run, we employed the low-resolution version, where the mass resolution $m_{\text{gas}} = 5.6 \times 10^4 M_{\odot}$. We evolve the galaxy down to $z = 2$, when the metallicity is already comparable to that of our dwarf galaxy at $z = 0$, and we repeat the analysis performed in Section 3.3. The [CII]–SFR and [OI]–SFR correlations are reported in the top and bottom panels of Fig. A2, respectively, at $z = 2$. In this case, to better highlight the trend of the distribution and limit the number of data points in the plot, the simulation data has been binned in annuli 500 pc wide, with the results shown as red dots. Because of the larger mass of the galaxy compared to our dwarf, SN feedback becomes less effective, and the gas can

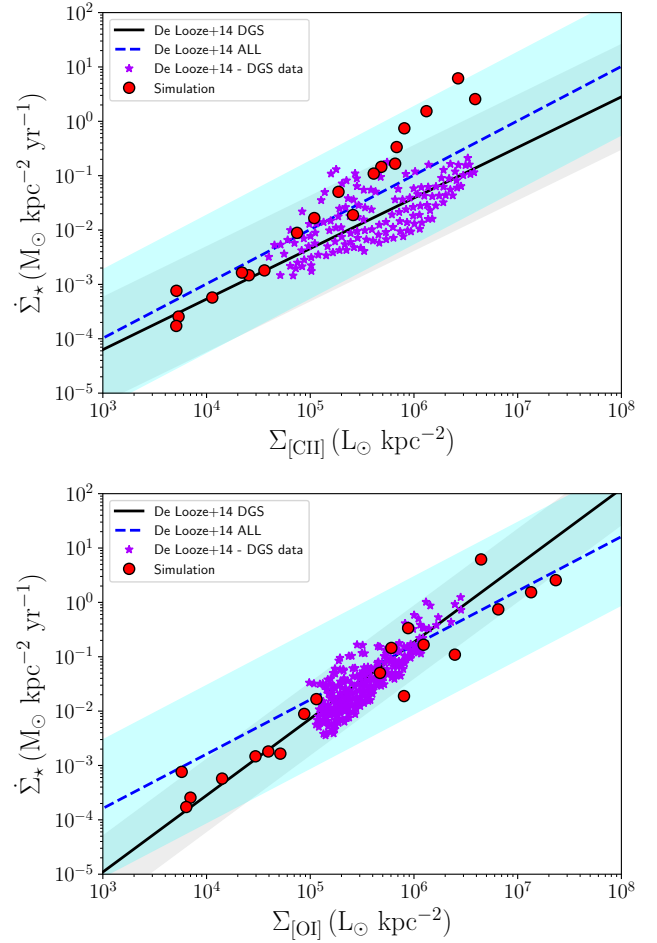


Figure A2. [CII]–SFR (top panel) and [OI]–SFR (bottom panel) correlations for the Milky Way-like halo. The purple stars correspond to the DGS galaxies by De Looze et al. (2014), with the black solid line (and the grey shaded area) representing the best-fit (and the 3σ scatter) over the DGS sample, and the blue dashed line (and the cyan shaded area) the best-fit to the entire literature sample by De Looze et al. (2014). Our simulation data, shown as red dots, exhibits a very good agreement with observations in both panels, because of the presence of dense regions in the galaxy where [OI] emission is much stronger. While the [OI] exhibits a consistent trend across the entire luminosity range, the [CII] counterpart shows a deficit at very-high luminosities. This deficit is due to the presence of very-high density gas in the central region of the galaxy, where the C⁺–C transition is efficient, and the [CII] emission is suppressed.

accumulate in the galaxy and more easily reach the typical densities where [OI] emission is powered.

Consistently with many observations of high-redshift galaxies, we also observe a [CII] deficit at very high luminosities, obviously not reproduced by the best-fit relation by De Looze et al. (2014). For what concerns the [OI] emission, instead, the agreement is very good across the entire luminosity interval. Although not reported, we also confirm the presence of an evolution of the integrated [CII]–SFR correlation with metallicity, similarly to the dwarf galaxy case. Concluding, the chemical network employed in this study works well also in cosmological simulations and is able to repro-

duce both the [CII]–SFR and [OI]–SFR correlations when the conditions to trigger efficient emission are met. Hence, the poorer agreement found in our dwarf galaxies is likely due to the lack of denser gas where the [OI] line is more efficiently excited, gas that is quickly dispersed by SN feedback. As a further comparison, we computed the [OI]/[CII] ratio for both dwarf and the Milky Way-like galaxies, finding an almost constant value across the entire SFR surface density interval sampled, as found in the Small Magellanic Cloud by [Jameson et al. \(2018\)](#). However, the ratio in our simulations is about unity, in better agreement with the results by [Herrera-Camus et al. \(2015\)](#) for low-metallicity systems.

This paper has been typeset from a \LaTeX file prepared by the author.